JOURNAL OF GUIDANCE, CONTROL, AND DYNAMICS
Vol. 30, No. 3, May–June 2007

Dynamics of Circularly Towed Cable Systems, Part 1: Optimal Configurations and Their Stability

Paul Williams* and Pavel Trivailo†
RMIT University, Melbourne, Victoria 3083, Australia

DOI: 10.2514/1.20433

When a long cable is towed in a circular flight path, the system can exhibit quasi-stationary solutions for which the cable tip appears to remain stationary relative to the orbiting aircraft. For applications involving pickup and delivery of payloads, tighter turns at high speeds lead to nearly stationary motion of the cable tip in an inertial frame. This work studies the dynamics of such a system, focusing on the stability and equilibria of solutions. A numerical analysis of the system is carried out using a discretized lumped mass model of the cable. By using constrained numerical optimization, practical towing solutions that achieve small motion of the towed body are obtained.

Nomenclature

$\boldsymbol{a}$	=	inertial acceleration vector, m/s^2
AR	=	aircraft aspect ratio
C_D	=	drag coefficient of cable segment or aircraft
$C_D A_d$	=	projected drag coefficient multiplied by drag area of towed body, m^2
C_f	=	cable skin-friction drag coefficient
C_L	=	lift coefficient of cable segment or aircraft
$C_{L_{\max}}$	=	maximum aircraft lift coefficient
C_{l_α}	=	two-dimensional aerofoil lift curve, rad
C_n	=	normal drag coefficient of cable segment
d	=	cable diameter, mm
e	=	aircraft span efficiency factor, 0.9
EA	=	cable stiffness, N
$\boldsymbol{e}_D$	=	unit vector in direction of cable element drag
$\boldsymbol{e}_L$	=	unit vector in direction of cable element lift
F^a	=	generalized aerodynamic forces on cable element, N
F^g	=	generalized gravitational forces on cable element, N
F^s	=	generalized elastic forces on cable element, N
F_t	=	aircraft thrust, N
g	=	gravitational constant at Earth sea level, 9.81 m/s^2
h	=	aircraft altitude, m
L	=	length used to normalize cable elements, m
l	=	length of cable element, m
L_s	=	unstrained cable element length, m
L_t	=	total cable length, m
m	=	aircraft mass, kg
m_j	=	mass of jth cable element, kg
M_n	=	Mach number of flow normal to the cable element
M_p	=	Mach number of flow parallel to the cable element
n	=	total number of cable elements
n_L	=	load factor on aircraft
P	=	aircraft power required, W
$\bar{q}$	=	dynamic pressure of flow at aircraft, N/m^2
r	=	aircraft orbit radius, m
r_d	=	towed-body orbit radius, m
S	=	aircraft wing area, m^2
T	=	cable tension, N
V	=	aircraft speed, m/s
$\boldsymbol{v}$	=	inertial speed vector, m/s
α	=	generalized coordinate describing angular rotation of cable element, rad
$\alpha^{a/c}$	=	aircraft angle of attack, rad
$\alpha_0^{a/c}$	=	aircraft zero-lift angle of attack, deg
β	=	generalized coordinate describing angular rotation of cable element, rad
γ	=	aircraft flight-path angle, rad
θ	=	aircraft angular position in orbit, rad
ϑ	=	angle of attack of cable element, rad
Λ	=	nondimensional length of cable element, l/L
λ	=	eigenvalues of linearized system plant matrix
ρ	=	density of air or cable material, kg/m^3
σ_{ut}	=	ultimate tensile strength of cable material, N/m^2
ϕ	=	aircraft bank angle, rad
ω	=	orbital angular velocity of aircraft, rad/s

Subscript

j	=	jth cable element

Superscripts

$\cdot$	=	time derivative, d()/dt
$'$	=	nondimensional time derivative, d()/d(ωt)

I. Introduction

TOWED-CABLE systems have several potential applications in both civilian and military environments. Cables towed from an aircraft can be used for remote sensing, towing decoys, and possibly even "snatch" pickup of payloads. Some of these applications and their associated dynamics and control have been studied previously [1–3]. One application of towed-cable systems that has not only been studied, but confirmed through flight tests, is the ability to obtain near-stationary motions of the cable tip by flying the aircraft in a tight circular path. This concept was first demonstrated by a pilot of the Missionary Aviation Fellowship, Nate Saint, in the 1950s. The presence of cable drag, and a reasonably large drag to weight ratio on the end body, causes the cable tip to move towards the center of the circle as the aircraft orbits. For certain combinations of the system parameters (tow speed, circle radius, cable length) the cable takes up a stable configuration with the cable tip almost stationary in an inertial frame. This idea was used by Nate Saint to deliver and receive gifts from Indians in Ecuador.

The purpose of this paper is to study the dynamics of a towed-cable system for the case where the cable is towed from a circling aircraft. The work presented here extends previous analyses (see Sec. II for a

Presented as Paper 6124 at the AIAA Atmospheric Flight Mechanics, San Francisco, 15–18 August 2005; received 8 October 2005; revision received 27 February 2006; accepted for publication 1 March 2006.

*Research Fellow, School of Aerospace, Mechanical, and Manufacturing Engineering, P.O. Box 71; paul.williams@rmit.edu.au. Member AIAA.

†Professor, School of Aerospace, Mechanical, and Manufacturing Engineering, P.O. Box 71.

literature review) to consider optimal cable configurations that achieve the smallest possible motion of the cable tip in an inertial frame. The equilibrium solutions are obtained using a discrete shooting technique, and the corresponding stability of the solutions is studied by means of a linear analysis. Particular emphasis is placed on the physical requirements for the towing aircraft and how the cable configurations influence these requirements. The structure of the paper is as follows: First, a lumped mass model of the cable is derived for the circularly towed configuration; next, the nominal equilibrium configurations and their stability are studied; finally, the implications for engineering design are assessed.

II. Literature Review on Circularly Towed Systems

Studies on the dynamics of cables and strings towed in circular paths have been presented in the literature dating back to Euler and Bernoulli for the drag-free case. Euler derived solutions for the linearized eigenvalues of a cable spinning about its own axis in the absence of air drag. Drag-free nonlinear motion was subsequently studied by Kolodner [4] and Wu [5], who obtained asymptotic solutions. Caughey [6] analyzed the motion of the system when the towpoint moved in a circular path and studied the dynamical stability of the solutions. More recently, Coomer et al. [7] studied the nonlinear eigenvalues of whirling inextensible strings and compared results with those obtained from an experimental rig. Lemon and Fraser [8] extended this work to consider inextensible cables towed in a circular path subject to aerodynamic drag, but without an end mass attached. Instabilities were observed in the linearized problem for combinations of low drag and high rotational speeds.

Skop and Choo [9] investigated the equilibrium conditions and cable configuration for a cable towed in a circular path. The cable was assumed to be flexible, but inextensible. In determining the hydrodynamic loading on the cable, only the normal drag component was considered (the side and tangential components were set to zero). The drogue attached at the end of the cable was assumed to be spherical. For the airborne system example, added mass and buoyancy effects were neglected. Scaling laws for geometrically similar configurations were derived and results suggest that if the ratio of cable length to towpoint radius is less than 6, then the steady-state radius of the drogue's orbit will be greater than 80% of the towpoint's radius. For high values of $V/\sqrt{gd}$ there are multivalued solutions for the cable equilibrium configuration. Increasing the weight of the drogue was shown to decrease the multivalued region.

Russell and Anderson [10] studied a simplified model of the towed-cable system by treating the cable as a rigid rod connected to a single point mass, representing the end body. Even with these simplifications multivalued solutions were shown to occur for particular rotational velocities. The results are analogous to those of a hardening spring-mass system. It was also shown that dynamic instability can arise in the system even in the absence of aerodynamic drag. Russell and Anderson [11] also extended the study to consider flexible cables, observing jump phenomena and dynamic instabilities.

Zhu and Rahn [12] studied the stability of a circularly towed cable system by assuming small strains and by neglecting the tangential component of the cable drag. A Galerkin approximation was used to expand the cable vibrations into admissible coordinates, and the solution was linearized around the steady-state cable shape. Unique, stable solutions were found to occur for low rotational velocities, but multivalued solutions were reported for higher rotational speeds. By varying several properties of the system it was demonstrated that increasing the end body mass has a similar effect to decreasing the amount of aerodynamic drag on the system. Similar results were obtained by Cohen and Manor [13] for the case of helical vertical descent (i.e., the towpoint moves in a circle while simultaneously descending at constant velocity). A related study of ballooning strings subject to aerodynamic drag, i.e., where the top end is fixed and the bottom is rotated in a circular motion, was conducted by Zhu et al. [14]. Multiple loop solutions were obtained and validated experimentally. It was found that the steady-state tension tends to decrease as the number of loops increases. However, such solutions exhibit flutter and divergent instabilities.

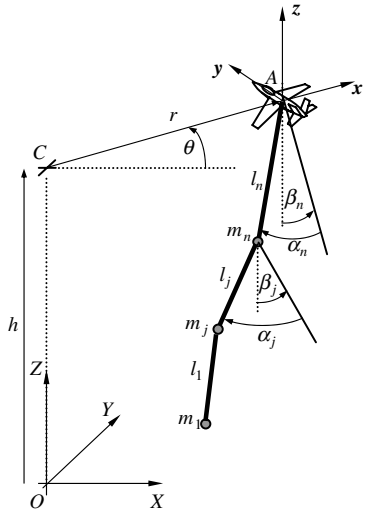

Fig. 1 Lumped mass representation of the cable dynamics.

The tension forces in aerial-towed systems were studied by Narkis [15] at the end of the deployment phase, which exhibits a peak in tension due to the sudden deceleration of the cable at full extension. Narkis developed an approximate analytical expression for the upper bound on the peak deployment stress assuming motion in the horizontal plane. Matuk [16] studied the peak forces in an aerial-cable system when the aircraft performs a 180 deg turn. The maximum tension force was found to occur after the aircraft completes the turn due to the "whip" effect of the cable. Twelve flight tests of the system were performed and the tension in the cable at the towing end was measured. The measured force was found to be consistently less than the theoretically predicted value.

Crist [17] studied the dynamics of a cable towed from a circling aircraft using a lumped mass model of the cable. Results for cases where the aircraft undergoes severe vertical oscillations and where the aircraft transitions from circling to straight level flight were presented. Equilibrium of the cable was first determined by assuming an altitude and radius for the drogue, allowing all forces except tension to be calculated. This process continues sequentially at each discrete mass point until the position of the aircraft is recovered. Numerical results show that a slack cable at the drogue is possible for a vertically oscillating aircraft, and this significantly affects the motion of the system. It is also shown that the tension in the cable can be significant as the aircraft transitions from orbit to straight flight.

Clifton et al. [18] studied the dynamics of a cable towed from a circling aircraft using a continuous model of the cable. It was assumed that the cable is inextensible, and only small motion around the cable equilibrium position was considered. Several checks of the accuracy of the model were made. The error in measured verticality with a flight test (E-6A TACAMO) was approximately 8%, although the oscillation, frequency, and phasing of the drogue verticality correlated quite well.

III. Mathematical Model for Towed-Cable System

The mathematical modeling of cable systems is well established in the literature on the subject for both air and space environments, as well as underwater environments [19–31]. Typically, a continuum model, or a discretized finite element or lumped mass representation of the cable dynamics is used. For combined ease of implementation and flexibility, a lumped mass model of the cable is used here. The cable dynamics are described in a rotating coordinate system (x, y, z) attached to the aircraft at A, as shown in Fig. 1. The aircraft motion is assumed to be planar and prescribed by the polar coordinates (r, θ). The (x, y, z) coordinate system rotates about the inertial Z-axis at the rate $\dot{\theta}$. The origin O of the inertial axes (X, Y, Z) is located at the center of the aircraft orbit at ground level. The aircraft orbits about the point C, located at altitude h directly above point O. The x-axis of the

local orbiting coordinate system is oriented with respect to the inertial X-axis by the angle θ.

The aircraft flight path is prescribed to be circular and at constant altitude. A constant aircraft altitude is desirable for payload delivery/retrieval applications because it limits the excitation of the cable tip in the vertical plane. Variations in altitude can easily be accommodated into the model, but studies of the effects are beyond the scope of this paper. For simplicity, the aircraft is treated as a point mass, and some of the important performance requirements such as bank angle, angle of attack, and required thrust are computed using the equations of motion for a point mass aircraft expressed in the rotating frame (see Sec. IV.B.1).

The continuous cable is discretized into n elements, which are assumed to have uniform unstrained lengths, $L_s = L_t/n$. The lumped masses are numbered sequentially from 1 at the drogue to n, representing the last deployed mass. The masses are connected via elastic springs that model the cable elasticity. The motion of each cable element is expressed in the rotating frame using spherical coordinates (l_j, α_j, β_j), $j = 1, \ldots, n$. The orientation angles are defined by two sequential right-handed rotations as follows (the cable segment is first parallel to the z-axis): the cable segment is first rotated about the x-axis by the angle β_j, followed by a rotation about the new y-axis by the angle α_j.

The position vector of the nth mass is given by

$$\boldsymbol{r}_n = (r - l_n \sin\alpha_n)\boldsymbol{i} - l_n \cos\alpha_n \sin\beta_n \boldsymbol{j} + (h - l_n \cos\alpha_n \cos\beta_n)\boldsymbol{k} \tag{1}$$

where $(\boldsymbol{i}, \boldsymbol{j}, \boldsymbol{k})$ are unit vectors in the (x, y, z)-directions, respectively. The positions of the remaining masses are determined sequentially as follows:

$$\boldsymbol{r}_j = \boldsymbol{r}_{j+1} - l_j \sin\alpha_j \boldsymbol{i} - l_j \cos\alpha_j \sin\beta_j \boldsymbol{j} - l_j \cos\alpha_j \cos\beta_j \boldsymbol{k}, \qquad j = n-1, \ldots, 1 \tag{2}$$

The corresponding inertial velocities are given by

$$\begin{aligned}\boldsymbol{v}_n = {} & (\dot{r} - \dot{l}_n \sin\alpha_n - l_n\dot{\alpha}_n \cos\alpha_n + l_n\dot{\theta}\cos\alpha_n \sin\beta_n)\boldsymbol{i} \\ & + (r\dot{\theta} - \dot{l}_n \cos\alpha_n \sin\beta_n + l_n\dot{\alpha}_n \sin\alpha_n \sin\beta_n - l_n\dot{\beta}_n \cos\alpha_n \cos\beta_n - l_n\dot{\theta}\sin\alpha_n)\boldsymbol{j} \\ & + (\dot{h} - \dot{l}_n \cos\alpha_n \cos\beta_n + l_n\dot{\alpha}_n \sin\alpha_n \cos\beta_n + l_n\dot{\beta}_n \cos\alpha_n \sin\beta_n)\boldsymbol{k}\end{aligned} \tag{3}$$

$$\begin{aligned}\boldsymbol{v}_j = \boldsymbol{v}_{j+1} & + (-\dot{l}_j \sin\alpha_j - l_j\dot{\alpha}_j \cos\alpha_j + l_j\dot{\theta}\cos\alpha_j \sin\beta_j)\boldsymbol{i} \\ & + (-\dot{l}_j \cos\alpha_j \sin\beta_j + l_j\dot{\alpha}_j \sin\alpha_j \sin\beta_j - l_j\dot{\beta}_j \cos\alpha_j \cos\beta_j - l_j\dot{\theta}\sin\alpha_j)\boldsymbol{j} \\ & + (-\dot{l}_j \cos\alpha_j \cos\beta_j + l_j\dot{\alpha}_j \sin\alpha_j \cos\beta_j + l_j\dot{\beta}_j \cos\alpha_j \sin\beta_j)\boldsymbol{k}\end{aligned} \tag{4}$$

The inertial accelerations are given by

$$\begin{aligned}\boldsymbol{a}_n = {} & (\ddot{r} - r\dot{\theta}^2 - \ddot{l}_n \sin\alpha_1 - 2\dot{l}_n\dot{\alpha}_n \cos\alpha_n - l_n\ddot{\alpha}_n \cos\alpha_n + l_n\dot{\alpha}_n^2 \sin\alpha_n + 2\dot{l}_n\dot{\theta}\cos\alpha_n \sin\beta_n + l_n\ddot{\theta}\cos\alpha_n \sin\beta_n - 2l_n\dot{\theta}\dot{\alpha}_n \sin\alpha_n \sin\beta_n \\ & + 2l_n\dot{\theta}\dot{\beta}_n \cos\alpha_n \cos\beta_n + l_n\dot{\theta}^2 \sin\alpha_n)\boldsymbol{i} + (r\ddot{\theta} + 2\dot{r}\,\dot{\theta} - \ddot{l}_n \cos\alpha_n \sin\beta_n + 2\dot{l}_n\dot{\alpha}_n \sin\alpha_n \sin\beta_n - 2\dot{l}_n\dot{\beta}_n \cos\alpha_n \cos\beta_n + l_n\ddot{\alpha}_n \sin\alpha_n \sin\beta_n \\ & + l_n\dot{\alpha}_n^2 \cos\alpha_n \sin\beta_n + 2l_n\dot{\alpha}_n\dot{\beta}_n \sin\alpha_n \cos\beta_n - l_n\ddot{\beta}_n \cos\alpha_n \cos\beta_n + l_n\dot{\beta}_n^2 \cos\alpha_n \sin\beta_n - 2\dot{l}_n\dot{\theta}\sin\alpha_n - l_n\ddot{\theta}\sin\alpha_n - 2l_n\dot{\theta}\dot{\alpha}_n \cos\alpha_n \\ & + l_n\dot{\theta}^2 \cos\alpha_n \sin\beta_n)\boldsymbol{j} + (\ddot{h} - \ddot{l}_n \cos\alpha_n \cos\beta_n + 2\dot{l}_n\dot{\alpha}_n \sin\alpha_n \cos\beta_n + 2\dot{l}_n\dot{\beta}_n \cos\alpha_n \sin\beta_n + l_n\ddot{\alpha}_n \sin\alpha_n \cos\beta_n + l_n\dot{\alpha}_n^2 \cos\alpha_n \cos\beta_n \\ & - 2l_n\dot{\alpha}_n\dot{\beta}_n \sin\alpha_n \sin\beta_n + l_n\ddot{\beta}_n \cos\alpha_n \sin\beta_n + l_n\dot{\beta}_n^2 \cos\alpha_n \cos\beta_n)\boldsymbol{k}\end{aligned} \tag{5}$$

$$\begin{aligned}\boldsymbol{a}_j = \boldsymbol{a}_{j+1} & + (-\ddot{l}_j \sin\alpha_j - 2\dot{l}_j\dot{\alpha}_j \cos\alpha_j - l_j\ddot{\alpha}_j \cos\alpha_j + l_j\dot{\alpha}_j^2 \sin\alpha_j + 2\dot{l}_j\dot{\theta}\cos\alpha_j \sin\beta_j + l_j\ddot{\theta}\cos\alpha_j \sin\beta_j - 2l_j\dot{\theta}\dot{\alpha}_j \sin\alpha_j \sin\beta_j \\ & + 2l_j\dot{\theta}\dot{\beta}_j \cos\alpha_j \cos\beta_j + l_j\dot{\theta}^2 \sin\alpha_j)\boldsymbol{i} + (-\ddot{l}_j \cos\alpha_j \sin\beta_j + 2\dot{l}_j\dot{\alpha}_j \sin\alpha_j \sin\beta_j - 2\dot{l}_j\dot{\beta}_j \cos\alpha_j \cos\beta_j + l_j\ddot{\alpha}_j \sin\alpha_j \sin\beta_j \\ & + l_j\dot{\alpha}_j^2 \cos\alpha_j \sin\beta_j + 2l_j\dot{\alpha}_j\dot{\beta}_j \sin\alpha_j \cos\beta_j - l_j\ddot{\beta}_j \cos\alpha_j \cos\beta_j + l_j\dot{\beta}_j^2 \cos\alpha_j \sin\beta_j - 2\dot{l}_j\dot{\theta}\sin\alpha_j - l_j\ddot{\theta}\sin\alpha_j - 2l_j\dot{\theta}\dot{\alpha}_j \cos\alpha_j \\ & + l_j\dot{\theta}^2 \cos\alpha_j \sin\beta_j)\boldsymbol{j} + (-\ddot{l}_j \cos\alpha_j \cos\beta_j + 2\dot{l}_j\dot{\alpha}_j \sin\alpha_j \cos\beta_j + 2\dot{l}_j\dot{\beta}_j \cos\alpha_j \sin\beta_j + l_j\ddot{\alpha}_j \sin\alpha_j \cos\beta_j + l_j\dot{\alpha}_j^2 \cos\alpha_j \cos\beta_j \\ & - 2l_j\dot{\alpha}_j\dot{\beta}_j \sin\alpha_j \sin\beta_j + l_j\ddot{\beta}_j \cos\alpha_j \sin\beta_j + l_j\dot{\beta}_j^2 \cos\alpha_j \cos\beta_j)\boldsymbol{k}\end{aligned} \tag{6}$$

The equations of motion may be expressed in the form

$$\boldsymbol{a}_j = \frac{\boldsymbol{F}_j}{m_j}, \qquad j = 1, \ldots, n \tag{7}$$

The second derivatives of the generalized coordinates for the jth mass are obtained by subtracting the components of $\boldsymbol{a}_{j+1}$ from $\boldsymbol{a}_j$ for $j = n-1, \ldots, 1$, and rearranging the resulting equations as follows:

$$\begin{aligned}\ddot{l}_n = {} & \ddot{h}\cos\alpha_n \cos\beta_n + \ddot{r}\sin\alpha_n + r\ddot{\theta}\cos\alpha_n \sin\beta_n + 2\dot{r}\,\dot{\theta}\cos\alpha_n \sin\beta_n - r\dot{\theta}^2 \sin\alpha_n + l_n\dot{\beta}_n^2\cos^2\alpha_n - l_n\dot{\theta}^2\cos^2\alpha_n\cos^2\beta_n + l_n\dot{\alpha}_n^2 + l_n\dot{\theta}^2 \\ & - 2l_n\dot{\theta}\dot{\alpha}_n \sin\beta_n + 2l_n\dot{\theta}\dot{\beta}_n \sin\alpha_n \cos\alpha_n \cos\beta_n - \frac{F^{\text{total}}_{3(n-1)+1}}{m_n}\sin\alpha_n - \frac{F^{\text{total}}_{3(n-1)+2}}{m_n}\cos\alpha_n \sin\beta_n - \frac{F^{\text{total}}_{3(n-1)+3}}{m_n}\cos\alpha_n \cos\beta_n\end{aligned} \tag{8}$$

$$\ddot{\alpha}_n = -\frac{\ddot{h}}{l_n}\sin\alpha_n\cos\beta_n + \frac{\ddot{r}}{l_n}\cos\alpha_n - \frac{r\ddot{\theta}}{l_n}\sin\alpha_n\sin\beta_n - 2\frac{\dot{r}\,\dot{\theta}}{l_n}\sin\alpha_n\sin\beta_n + \ddot{\theta}\sin\beta_n - \frac{r\dot{\theta}^2}{l_n}\cos\alpha_n - 2\frac{\dot{l}_n\dot{\alpha}_n}{l_n} + 2\frac{\dot{l}_n\dot{\theta}}{l_n}\sin\beta_n + 2\dot{\theta}\dot{\beta}_n\cos^2\alpha_n\cos\beta_n + \dot{\theta}^2\sin\alpha_n\cos\alpha_n\cos^2\beta_n - \dot{\beta}_n^2\sin\alpha_n\cos\alpha_n - \frac{F^{\text{total}}_{3(n-1)+1}}{m_n l_n}\cos\alpha_n + \frac{F^{\text{total}}_{3(n-1)+2}}{m_n l_n}\sin\alpha_n\sin\beta_n + \frac{F^{\text{total}}_{3(n-1)+3}}{m_n l_n}\sin\alpha_n\cos\beta_n \tag{9}$$

$$\ddot{\beta}_n = -\frac{\ddot{h}}{l_n}\frac{\sin\beta_n}{\cos\alpha_n} + \frac{r\ddot{\theta}\cos\beta_n}{l_n\cos\alpha_n} + 2\frac{\dot{r}\,\dot{\theta}\cos\beta_n}{l_n\cos\alpha_n} - \frac{\ddot{\theta}\sin\alpha_n\cos\beta_n}{\cos\alpha_n} - 2\frac{\dot{l}_n\dot{\beta}_n}{l_n} - 2\frac{\dot{l}_n\dot{\theta}\sin\alpha_n\cos\beta_n}{l_n\cos\alpha_n} + 2\frac{\dot{\alpha}_n\dot{\beta}_n\sin\alpha_n}{\cos\alpha_n} + \dot{\theta}^2\sin\beta_n\cos\beta_n - 2\dot{\alpha}_n\dot{\theta}\cos\beta_n - \frac{F^{\text{total}}_{3(n-1)+2}}{m_n l_n}\frac{\cos\beta_n}{\cos\alpha_n} + \frac{F^{\text{total}}_{3(n-1)+3}}{m_n l_n}\frac{\sin\beta_n}{\cos\alpha_n} \tag{10}$$

$$\ddot{l}_j = l_j\dot{\beta}_j^2\cos^2\alpha_j - l_j\dot{\theta}^2\cos^2\alpha_j\cos^2\beta_j + l_j\dot{\alpha}_j^2 + l_j\dot{\theta}^2 - 2l_j\dot{\theta}\dot{\alpha}_j\sin\beta_j + 2l_j\dot{\theta}\dot{\beta}_j\sin\alpha_j\cos\alpha_j\cos\beta_j + \left(\frac{F^{\text{total}}_{3j+1}}{m_{j+1}} - \frac{F^{\text{total}}_{3(j-1)+1}}{m_j}\right)\sin\alpha_j + \left(\frac{F^{\text{total}}_{3j+2}}{m_{j+1}} - \frac{F^{\text{total}}_{3(j-1)+2}}{m_j}\right)\cos\alpha_j\sin\beta_j + \left(\frac{F^{\text{total}}_{3j+3}}{m_{j+1}} - \frac{F^{\text{total}}_{3(j-1)+3}}{m_j}\right)\cos\alpha_j\cos\beta_j \tag{11}$$

$$\ddot{\alpha}_j = \ddot{\theta}\sin\beta_j - 2\frac{\dot{l}_j\dot{\alpha}_j}{l_j} + 2\frac{\dot{l}_j\dot{\theta}}{l_j}\sin\beta_j + 2\dot{\theta}\dot{\beta}_j\cos^2\alpha_j\cos\beta_j + \dot{\theta}^2\sin\alpha_j\cos\alpha_j\cos^2\beta_j - \dot{\beta}_j^2\sin\alpha_j\cos\alpha_j + \left(\frac{F^{\text{total}}_{3j+1}}{m_{j+1}l_j} - \frac{F^{\text{total}}_{3(j-1)+1}}{m_j l_j}\right)\cos\alpha_j + \left(\frac{F^{\text{total}}_{3(j-1)+2}}{m_j l_j} - \frac{F^{\text{total}}_{3j+2}}{m_{j+1}l_j}\right)\sin\alpha_j\sin\beta_j + \left(\frac{F^{\text{total}}_{3(j-1)+3}}{m_j l_j} - \frac{F^{\text{total}}_{3j+3}}{m_{j+1}l_j}\right)\sin\alpha_j\cos\beta_j \tag{12}$$

$$\ddot{\beta}_j = -\frac{\ddot{\theta}\sin\alpha_j\cos\beta_j}{\cos\alpha_j} - 2\frac{\dot{l}_j\dot{\beta}_j}{l_j} - 2\frac{\dot{l}_j\dot{\theta}\sin\alpha_j\cos\beta_j}{l_j\cos\alpha_j} + 2\frac{\dot{\alpha}_j\dot{\beta}_j\sin\alpha_j}{\cos\alpha_j} + \dot{\theta}^2\sin\beta_j\cos\beta_j - 2\dot{\alpha}_j\dot{\theta}\cos\beta_j + \left(\frac{F^{\text{total}}_{3j+2}}{m_{j+1}l_j} - \frac{F^{\text{total}}_{3(j-1)+2}}{m_j l_j}\right)\frac{\cos\beta_j}{\cos\alpha_j} + \left(\frac{F^{\text{total}}_{3(j-1)+3}}{m_j l_j} - \frac{F^{\text{total}}_{3j+3}}{m_{j+1}l_j}\right)\frac{\sin\beta_j}{\cos\alpha_j} \tag{13}$$

where

$$F^{\text{total}}_{3(j-1)+i} = F^s_{3(j-1)+i} + F^g_{3(j-1)+i} + F^a_{3(j-1)+i}, \quad i = 1,2,3; \qquad j = 1,\ldots,n \tag{14}$$

There are a number of important forces that appear in the right-hand side of Eq. (14). The most important forces that are considered in this work are tension s, gravity g, and aerodynamic a forces. No internal damping forces are considered in this paper. Internal damping forces affect the damping characteristics of the longitudinal vibrations of the cable, but do not have a significant effect on the stability of the transverse cable dynamics. Furthermore, the damping properties of different cable materials can vary widely and hence it is simpler to omit damping from the model for this study. Each of the remaining forces are described in the following subsections.

A. Force Models

1. Elastic Tension Forces

The tension in each spring element may be calculated by assuming that the material behaves according to Hooke's law. Note, however, that this is not a necessary assumption and that any force model can be used to represent the tension forces. The tension in the jth segment is expressed as

$$T_j = \frac{\text{EA}}{L_{s_j}}(l_j - L_{s_j}) \tag{15}$$

Note that it is assumed throughout this paper that $l_j > L_{s_j}$, i.e., that the cable maintains tension for small motions around the equilibrium position.

The tension forces may be written in component form as

$$\begin{aligned} F^s_{3(j-1)+1} &= T_j\sin\alpha_j - T_{j-1}\sin\alpha_{j-1} \\ F^s_{3(j-1)+2} &= T_j\cos\alpha_j\sin\beta_j - T_{j-1}\cos\alpha_{j-1}\sin\beta_{j-1} \\ F^s_{3(j-1)+3} &= T_j\cos\alpha_j\cos\beta_j - T_{j-1}\cos\alpha_{j-1}\cos\beta_{j-1} \end{aligned} \qquad (j = 1,\ldots,n) \tag{16}$$

where it is recognized that $T_0 = 0$.

2. Gravity Forces

In this work, gravity is assumed to be invariant with altitude so that

$$\begin{aligned} F^g_{3(j-1)+1} &= 0 \\ F^g_{3(j-1)+2} &= 0 \\ F^g_{3(j-1)+3} &= -m_j g \end{aligned} \qquad (j = 1,\ldots,n) \tag{17}$$

3. Aerodynamic Drag

The aerodynamic forces acting on the cable can be determined from the crossflow principle [32]. For efficient computation, the aerodynamic forces on the jth mass are calculated by using the orientation of the $(j-1)$th segment and the velocity of the jth mass.

The lift and drag coefficients for an inclined cylinder are given by [32]

$$C_{D_j} = C_{f_j} + C_{n_j}\sin^3\vartheta_j \tag{18}$$

$$C_{L_j} = C_{n_j}\sin^2\vartheta_j\cos\vartheta_j \tag{19}$$

where the skin-friction and crossflow drag coefficients are taken to be [33]

$$C_{f_j} = \begin{cases} 0.038 - 0.0425M_{p_j}, & M_{p_j} < 0.4 \\ 0.013 + 0.0395(M_{p_j} - 0.85)^2, & M_{p_j} \geq 0.4 \end{cases} \tag{20}$$

$$C_{n_j} = 1.17 + M_{n_j}/40 - M_{n_j}^2/4 + 5M_{n_j}^2/8 \tag{21}$$

The angle of attack of the jth segment may be calculated from

$$\cos\vartheta_j = \frac{-\boldsymbol{l}_j \cdot \boldsymbol{v}_j}{|\boldsymbol{l}_j||\boldsymbol{v}_j|} = \frac{v_{x_j}\sin\alpha_j + v_{y_j}\cos\alpha_j\sin\beta_j + v_{z_j}\cos\alpha_j\cos\beta_j}{\sqrt{(v_{x_j})^2 + (v_{y_j})^2 + (v_{z_j})^2}} \tag{22}$$

where

$$\boldsymbol{l}_j = -l_j\sin\alpha_j\boldsymbol{i} - l_j\cos\alpha_j\sin\beta_j\boldsymbol{j} - l_j\cos\alpha_j\cos\beta_j\boldsymbol{k} \tag{23}$$

The unit vectors defining the directions of the lift and drag vectors are

$$\boldsymbol{e}_D = -\frac{\boldsymbol{v}_j}{|\boldsymbol{v}_j|} \tag{24}$$

$$\boldsymbol{e}_L = -\frac{(\boldsymbol{v}_j \times \boldsymbol{l}_j)\times\boldsymbol{v}_j}{|(\boldsymbol{v}_j \times \boldsymbol{l}_j)\times\boldsymbol{v}_j|} \tag{25}$$

Equation (25) can be expressed in component form as

$$\boldsymbol{e}_L = \frac{\eta_{3(j-1)+1}\boldsymbol{i} + \eta_{3(j-1)+2}\boldsymbol{j} + \eta_{3(j-1)+3}\boldsymbol{k}}{\sqrt{\eta^2_{3(j-1)+1} + \eta^2_{3(j-1)+2} + \eta^2_{3(j-1)+3}}} \tag{26}$$

where

$$\eta_{3(j-1)+1} = (v_{z_j}\sin\alpha_j - v_{x_j}\cos\alpha_j\cos\beta_j)v_{z_j} + (v_{y_j}\sin\alpha_j - v_{x_j}\cos\alpha_j\sin\beta_j)v_{y_j} \tag{27}$$

$$\eta_{3(j-1)+2} = (v_{x_j}\cos\alpha_j\sin\beta_j - v_{y_j}\sin\alpha_j)v_{x_j} + (v_{z_j}\cos\alpha_j\sin\beta_j - v_{y_j}\cos\alpha_j\cos\beta_j)v_{z_j} \tag{28}$$

$$\eta_{3(j-1)+3} = (v_{y_j}\cos\alpha_j\cos\beta_j - v_{z_j}\cos\alpha_j\sin\beta_j)v_{x_j} + (v_{x_j}\cos\alpha_j\cos\beta_j - v_{z_j}\sin\alpha_j)v_{x_j} \tag{29}$$

Hence, the lift and drag vectors may be written as

$$\boldsymbol{F}_j^{\text{drag}} = \frac{1}{2}\rho_j C_{D_j} L_{s_j} d|\boldsymbol{v}_j|^2\boldsymbol{e}_D = -\frac{1}{2}\rho_j C_{D_j} L_{s_j} d|\boldsymbol{v}_j|[v_{x_j}\boldsymbol{i} + v_{y_j}\boldsymbol{j} + v_{z_j}\boldsymbol{k}] \tag{30}$$

$$\boldsymbol{F}_j^{\text{lift}} = \frac{1}{2}\rho_j C_{L_j} L_{s_j} d|\boldsymbol{v}_j|^2\boldsymbol{e}_L = \frac{1}{2}\rho_j C_{L_j} L_{s_j} d|\boldsymbol{v}_j|^2\left(\frac{\eta_{3(j-1)+1}\boldsymbol{i} + \eta_{3(j-1)+2}\boldsymbol{j} + \eta_{3(j-1)+3}\boldsymbol{k}}{\sqrt{\eta^2_{3(j-1)+1} + \eta^2_{3(j-1)+2} + \eta^2_{3(j-1)+3}}}\right) \tag{31}$$

Thus the total aerodynamic force on the jth mass is given by

$$F^a_{3(j-1)+1} = (\boldsymbol{F}_j^{\text{drag}} + \boldsymbol{F}_j^{\text{lift}})\cdot\boldsymbol{i},\quad F^a_{3(j-1)+2} = (\boldsymbol{F}_j^{\text{drag}} + \boldsymbol{F}_j^{\text{lift}})\cdot\boldsymbol{j},\quad F^a_{3(j-1)+3} = (\boldsymbol{F}_j^{\text{drag}} + \boldsymbol{F}_j^{\text{lift}})\cdot\boldsymbol{k} \tag{32}$$

The aerodynamic drag of the towed body (drogue) is calculated based on a spherical shape and the air density is calculated based on the international standard atmosphere.

B. Nondimensional Equations

For numerical computation purposes, it is convenient to nondimensionalize the governing equations of the system. Assuming that the towpoint undergoes nonuniform angular rotation about the origin, it is convenient to change the independent variable from time to the angle θ. In the case of a uniform circular orbit, the nondimensional time can be expressed as $\theta = \omega t$. The cable segment lengths are nondimensionalized with respect to a scale length L such that $\Lambda_j = l_j/L$. The equations of motion for a uniform circular orbit in nondimensional variables are given in Appendix A.

IV. Equilibrium Conditions and Practical Aircraft Performance Limitations

A. Equilibrium Configurations

Equilibrium solutions for the towed-cable problem have been discussed at length in previous studies. Most notably, Skop and Choo [9], Russell and Anderson [11], and Clifton et al. [18] studied the equilibrium configurations and corresponding stability for the cable towed in a circular path. However, very little emphasis has been given to aircraft performance limitations in actually achieving some of the equilibrium solutions. To determine the relative equilibrium of the cable, the equations of motion for the lumped mass model of the cable are used. One approach is to specify the motion of the towpoint and solve the resulting set of nonlinear equations to give zero relative velocity and acceleration of the cable. This can be achieved using robust nonlinear programming software such as SNOPT [34]. The limitation of this approach is that reasonably good guesses are needed for the positions of the masses and that convergence can be relatively slow. A much more efficient approach is to exploit the fact that the system is differentially flat [35] under some mild assumptions. The system is differentially flat if it is assumed that the aerodynamic forces are lumped to each mass only from an adjacent segment, as discussed in Sec. III.A.3. The output that categorizes the motion of the system is the drogue (end body). Because we are interested in steady-state solutions, we can specify the location of the drogue in the rotating coordinate system in terms of its (x, y, z)-coordinates. The position of the drogue uniquely determines all forces acting on it except the components of the tension force,

$$T_1 = -m_1 x_1\dot{\theta}^2 - F_1^a \qquad T_2 = -m_1 y_1\dot{\theta}^2 - F_2^a \qquad T_3 = m_1 g - F_3^a \tag{33}$$

For a given unstrained segment length, the tension determines the elongated segment length from Hooke's law,

$$l_1 = L_{s_1}\left(1 + \frac{\sqrt{T_1^2 + T_2^2 + T_3^2}}{\text{EA}}\right) \tag{34}$$

and the position of the next mass may be determined as

$$x_j = x_{j-1} + \frac{T_1}{\sqrt{T_1^2 + T_2^2 + T_3^2}}l_1,\quad y_j = y_{j-1} + \frac{T_2}{\sqrt{T_1^2 + T_2^2 + T_3^2}}l_1,\quad z_j = z_{j-1} + \frac{T_3}{\sqrt{T_1^2 + T_2^2 + T_3^2}}l_1 \tag{35}$$

In general, the tension in the jth segment may be determined from the equations

$$T_{3(j-1)+1} = -m_j x_j\dot{\theta}^2 - F^a_{3(j-1)+1} + T_{3(j-2)+1},\quad T_{3(j-1)+2} = -m_j y_j\dot{\theta}^2 - F^a_{3(j-1)+2} + T_{3(j-2)+2},\quad T_{3(j-1)+3} = m_j g - F^a_{3(j-1)+3} + T_{3(j-2)+3} \tag{36}$$

Following this procedure allows the position of the towpoint to be obtained for a prescribed orbit radius of the drogue. The accuracy of the solution increases as the number of segments representing the cable increases. The validity of the solution is checked by converting the Cartesian coordinates of the masses into the generalized coordinates (Λ, α, β) and substituting the results into the dynamical equations for a prescribed towpoint motion. If the resulting

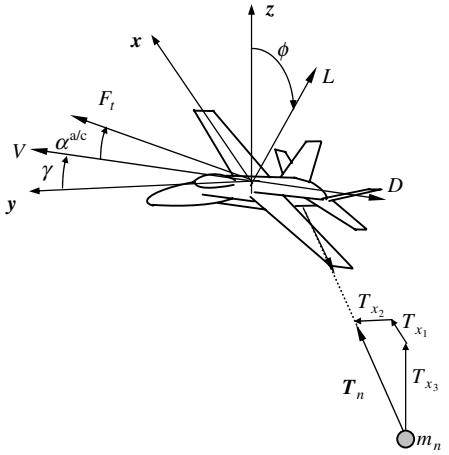

Fig. 2 Aircraft model in cylindrical coordinates.

accelerations are small, i.e., of the order 10^{-9}, then the solution is deemed to be accurate. Note that to convert the solution to the lumped mass model requires that the towpoint lie on the x-axis at radius r. It is a simple matter to apply a coordinate transformation to the equilibrium solution in the (x, y)-plane.

B. Practical Limitations on the Towing Maneuver

Insomuch as equilibrium solutions and their stability are mathematically interesting, the purpose of this section is to examine practical towing scenarios. Because the towpoint in this scenario is an aircraft, it is necessary to take into consideration the practical limitations imposed by the aircraft. Some of the key parameters limiting the practicality of the tow maneuver are 1) aircraft stall limit, 2) maximum bank angle/load factor, and 3) thrust or power requirements. All of these factors are strongly influenced by the type of aircraft used and its design parameters. In the following analysis, we treat the case of equilibrium with respect to the forces acting on the aircraft (including the cable tension forces).

1. *Aircraft Model*

The equilibrium of the aircraft is obtained by first formulating the equations of motion for an aircraft in cylindrical coordinates. For simplicity, a point mass model of the aircraft is used (see Fig. 2). The equations of motion can be written as

$$m(\ddot{r} - r\dot{\theta}^2) = -F_t \sin\alpha^{a/c} \sin\phi - \bar{q}SC_L \sin\phi - T_{x_1}^{(n)} \tag{37}$$

$$m(r\ddot{\theta} + 2\dot{r}\,\dot{\theta}) = (F_t \cos\alpha^{a/c} - \bar{q}SC_D)\cos\gamma - (F_t \sin\alpha^{a/c} \cos\phi + \bar{q}SC_L \cos\phi)\sin\gamma - T_{x_2}^{(n)} \tag{38}$$

$$m\ddot{h} = (F_t \cos\alpha^{a/c} - \bar{q}SC_D)\sin\gamma + (F_t \sin\alpha^{a/c} \cos\phi + \bar{q}SC_L \cos\phi)\cos\gamma - mg - T_{x_3}^{(n)} \tag{39}$$

where $T_{x_i}^{(n)}$ is the component of the tension force in the nth segment direct positively away from mass m_n (i.e., pointed towards the aircraft, as shown in Fig. 2).

2. *Equilibrium Conditions*

The equations of motion for the aircraft, Eqs. (37–39), can be used to define the equilibrium conditions for the aircraft when it is in a steady banked turn, i.e., when $\dot{r} = \ddot{r} = \ddot{\theta} = \gamma = \ddot{h} = 0$. Hence the equilibrium conditions are given by

$$mV^2/r = F_t \sin\alpha^{a/c} \sin\phi + \bar{q}SC_L \sin\phi + T_{x_1}^{(n)} \tag{40}$$

$$F_t \cos\alpha^{a/c} - \bar{q}SC_D - T_{x_2}^{(n)} = 0 \tag{41}$$

$$F_t \sin\alpha^{a/c} \cos\phi + \bar{q}SC_L \cos\phi - mg - T_{x_3}^{(n)} = 0 \tag{42}$$

Although the required bank angle for an aircraft in a turn is conventionally independent of the mass of the aircraft, the presence of a towing cable introduces a dependency as follows

$$\tan\phi = \frac{mV^2/r - T_{x_1}^{(n)}}{mg + T_{x_3}^{(n)}} \tag{43}$$

Equations (41) and (42) must be solved simultaneously for the angle of attack and thrust. Because the equations are nonlinear in the variables, an iterative approach is required. We have employed a Newton scheme with initial guesses based on neglecting the vertical component of the thrust:

$$C_L^{\text{guess}} = \frac{mg + T_{x_3}^{(n)}}{\bar{q}S\cos\phi} \tag{44}$$

$$F_t^{\text{guess}} = \bar{q}SC_D + T_{x_2}^{(n)} \tag{45}$$

For the aerodynamic performance, the lift and drag coefficients are assumed to be of the form

$$\begin{aligned} C_D &= C_{D_0} + KC_L^2 \\ &\approx \frac{S_{\text{wet}}}{S}C_{\text{fe}} + \frac{4}{3}\frac{1}{\pi e\text{AR}} \\ C_L &= C_{L_\alpha}(\alpha^{a/c} - \alpha_0^{a/c}) \\ &\approx \frac{C_{l_\alpha}}{C_{l_\alpha}/\pi\text{AR} + \sqrt{1 + (C_{l_\alpha}/\pi\text{AR})^2}}(\alpha^{a/c} - \alpha_0^{a/c}) \end{aligned} \tag{46}$$

3. *Stall Limit*

One of the most important practical limitations of the towing maneuver is the aircraft stall limit. The design factor influencing this is the maximum lift coefficient of the aircraft. This can be augmented somewhat through proper design of the aircraft using high-lift devices, but for the purposes here is assumed to be limited to a value of 1.1.

4. *Thrust/Power Limit*

When the aircraft operates at high angles of attack, a significant amount of lift-induced drag is generated, which requires high levels of thrust or power from the engine. The required thrust is calculated from the force balance, and the equivalent power required is calculated via $P = F_t V$.

5. *Load Factor*

When the aircraft operates at high load factors, $n_L = \bar{q}SC_L/(mg + T_{x_3}^{(n)})$, there is the potential for structural damage or pilot blackout. Although the limit load factor can be increased by appropriate design, we assume that it is limited to 4.0.

C. Stability of Equilibrium Solutions

The results from the preceding sections may be used to provide a quantitative assessment of the stability of different configuration tow maneuvers. A linear analysis is employed to determine the stability of the cable system for small motions around the equilibrium configuration. Such an analysis uses a linear approximation of the system plant matrix to calculate its eigenvalues λ and corresponding eigenvectors. Instead of performing the linearization analytically, it is calculated using a central finite difference approximation (see Appendix B). The eigenvalues and corresponding eigenvectors for the linearized cable dynamics may be calculated by assuming exponential motion and solving the resulting eigenvalue problem using the linearized plant matrix. The eigenvalues appear as either distinct real numbers (nonoscillatory motion) or as pairs of complex

Table 1 Material properties of cable

Material	Density, kg/m^3	Young's modulus E, GPa	Ultimate tensile strength, MPa	Strength-to-weight σ_{ut}/ρ
Steel	7850	200	570	0.0726
Aluminium	2750	70	200	0.0727
Nylon	1040	1	30	0.0288
Spectra	970	120	3200	3.2990
Plasma	840	37.4	450	0.5357

conjugates (oscillatory motion). The natural frequencies and damping ratios may be extracted from the real and imaginary parts of the eigenvalues. For stability of the linear system, it is necessary that the real parts of all the eigenvalues be negative. If the real part of the eigenvalue is positive and the imaginary part is zero, then the mode is an unstable divergent mode. If the real part of the eigenvalue is positive and the imaginary part is nonzero, then the mode corresponds to a flutter instability.

V. Numerical Results

To understand the basic performance characteristics of a circularly towed system, parametric studies of cable equilibrium configurations, the aircraft requirements, and the stability of the configurations were performed. Because there is a coupling between the aircraft performance parameters, such as mass, thrust, and so on, different typical aircraft configurations were selected for study. In addition to the aircraft, the cable material properties can have a strong influence on the solutions and so a variety of different cable materials were originally considered. Three aircraft configurations were selected for study. The first was similar to the P-3C Orion aircraft, whose main performance factors impacting the mission being considered are $m = 30,000$ kg, $b = 30.37$ m, $S = 120.77$ m^2, and $P_{\max} = 19,640$ hp (all engines operational). The second aircraft was selected as a light aircraft, similar to something that Nate Saint used originally: $m = 2000$ kg, $b = 9$ m, $S = 20$ m^2, and $P_{\max} = 300$ hp. The last aircraft is selected as a high performance military aircraft with parameters $m = 12,000$ kg, $b = 11.43$ m, $S = 37.2$ m^2, and $T_{\max} = 160$ kN. Note that these values are taken as rough estimates only. Some of the performance requirements depend on the drag characteristics of the aircraft, which have been estimated very crudely here. However, the method can be used with any aircraft parameters, which should prove useful for more detailed design for specific aircraft configurations.

The properties of the cable material for several different materials are shown in Table 1. Steel has been a commonly used material for towing cables, presumably because of its relatively high strength compared with materials that were previously available. However, with the advent of new fibers, such as Spectra, steel is no longer the material of choice. In fact, there are several good reasons for not selecting a material such as steel for the task. Not only does it have a relatively low strength-to-weight ratio compared with modern fibers, but it is susceptible to lightning strikes. In fact, the drive towards a lightweight cable was shown in initial performance results to be the most beneficial for the proposed maneuver.

A. Equilibrium Solutions of Cable System

Previous research has illustrated that, for the towed system to be effective in providing near-stationary motion, long, lightweight cables connected to light, high-drag end bodies are required [36]. For a given system geometry, small drogue tow radii are achievable by flying in circles with small radius and high angular velocity. The focus of many past studies has been on the mathematical nature of the solutions, i.e., possible multivalued solution regions, and so on. However, such solutions are not of practical interest here because they are generally beyond practical aircraft limitations. Therefore, focus is placed upon the aircraft constraints and the likely range of variables for which small drogue orbit radii are possible.

Comparisons of the different aircraft and material properties were performed with several key system parameters held fixed: $L = 3000$ m, $m_d = 10$ kg, $C_D A_d = 2.0$ m^2, and $d = 1$ mm. However, as expected, Spectra proved to provide the best performance compared with the other materials, so only results from it will be presented. Figure 3 shows the radius of the drogue's orbit for different towpoint velocities and different angular velocities for a cable discretization of 200 masses. A high angular velocity with low speed implies a towpoint circle with small radius. Note that these results do not incorporate the aircraft performance constraints, but merely illustrate what would be achievable for the given system geometry. In other words, they are valid for a given towing motion.

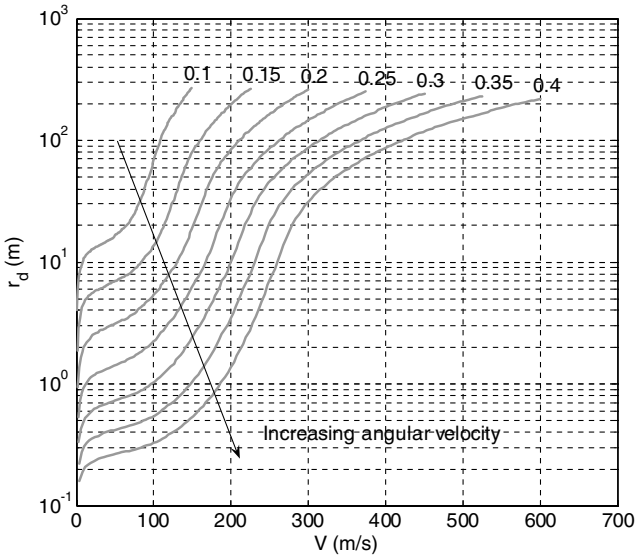

Fig. 3 Drogue orbit radius vs towpoint velocity for different angular velocities (rad/s).

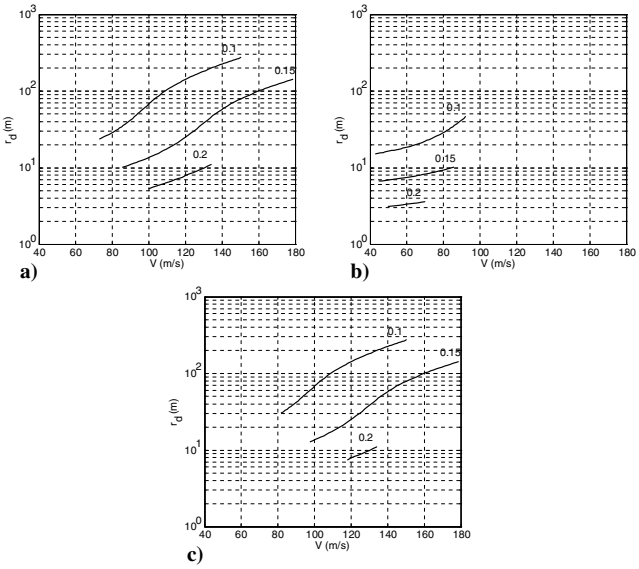

Fig. 4 Achievable drogue radii with aircraft performance constraints: a) Orion, b) light, and c) fighter aircraft.

Figure 3 clearly shows that to obtain small drogue orbit radii circles with small radius at high angular velocity need to be flown. If one accepts that a drogue orbit radius on the order of 10 m is acceptable, then it is clear that there is a large range of velocities and towpoint radii that can achieve the desired result.

Figure 4 shows the results from Fig. 3, emphasizing the range of achievable results for each aircraft given the performance constraints ($C_{L_{\max}} = 1.1$, $\phi_{\max} = 70$ deg, and $n_{L\max} = 4$). Only angular velocities of 0.1, 0.15, and 0.2 rad/s produced results that could be "flown" by each aircraft. Comparing Figs. 3 and 4, it is clear that the aircraft operational constraints severely restrict the range of possible drogue radii. The results suggest that a lighter aircraft is better able to achieve small drogue radii, primarily due to the improved stall limit because of the lighter aircraft mass. However, all three aircraft are capable of achieving the desired performance, but the Orion and light aircraft appear to be superior to a fighter-type aircraft.

B. Optimal Configurations and Their Stability

Varying the system angular velocity and orbit radius provides a systematic way of studying the influence of these key parameters on the system performance. However, this is a very time-consuming process and still does not give the best design point. In addition, the selection of the cable diameter affects not only the cable drag, but the cable tension because of the combination of drag and cable mass. For the cable to be able to sustain the loads it is subjected to, it must have a sufficient diameter. Therefore, there is an iterative process that needs to take place for each design combination. Because it is expected that the system will need to operate very close to the constraints, it is necessary to seek the optimum design with more efficiency. Various optimization methods are available to help find the optimum design point. Among them are genetic algorithms, simulated annealing, particle swarm methods, and sequential quadratic programming. Although the first three methods are very good at finding global minima in cases where the cost function may have multiple minima, they are not particularly good for finding solutions that lie on constraint surfaces. Hence, the sequential quadratic programming software SNOPT [34] has been selected as the optimizer.

The optimization problem is defined as follows: Find the aircraft orbit radius r, its angular velocity ω, and the cable diameter d to minimize the cost function

$$\mathcal{J} = r_d^2 \tag{47}$$

subject to the constraints

$$d \geq \sqrt{\frac{4|\boldsymbol{T}|_{\max}}{\pi\sigma_{\text{ut}}}}, \qquad \phi \leq \phi_{\max}, \qquad C_L \leq C_{L_{\max}},$$
$$n \leq n_{\max} \qquad F_t \leq F_{t\max} \quad \text{or} \quad P \leq P_{\max} \tag{48}$$

Table 2 Optimal design parameters for towed-circular system

Case	Orion			Light aircraft			Fighter		
	r, m	ω, rad/s	d, mm	r, m	ω, rad/s	d, mm	r, m	ω, rad/s	d, mm
Baseline	468.05	0.240	1.39	213.78	0.246	1.27	565.61	0.218	1.28
$m_d = 50$ kg	483.01	0.236	2.85	220.93	0.233	2.36	587.01	0.214	2.63
$m_d = 100$ kg	488.60	0.235	3.94	229.55	0.220	2.75	595.37	0.213	3.71
$m_d = 500$ kg	497.22	0.234	8.13	——	——	——	608.01	0.212	8.14
$C_D A_d = 0.5$ m^2	468.44	0.240	1.34	213.78	0.246	1.27	567.21	0.218	1.18
$C_D A_d = 1.0$ m^2	168.28	0.240	1.36	213.78	0.246	1.27	566.21	0.218	1.24
$C_D A_d = 3.0$ m^2	467.94	0.240	1.40	213.78	0.246	1.28	565.47	0.218	1.28
$L = 1$ km	401.19	0.259	0.65	168.84	0.291	2.29	493.22	0.234	0.87
$L = 2$ km	430.37	0.250	1.11	186.40	0.279	1.57	529.59	0.226	0.76
$L = 4$ km	514.19	0.229	1.24	242.04	0.225	1.10	615.81	0.209	1.34
$L = 5$ km	565.05	0.218	1.11	275.49	0.204	0.99	673.32	0.200	1.22
$\phi_{\max} = 40$ deg	667.67	0.111	1.95	262.81	0.178	1.57	815.91	0.100	1.01
$\phi_{\max} = 50$ deg	570.81	0.143	1.86	221.63	0.230	1.37	688.27	0.130	1.49
$\phi_{\max} = 60$ deg	508.84	0.183	1.63	213.78	0.246	1.27	613.53	0.166	1.50
$C_{L_{\max}} = 1.3$	402.73	0.259	1.35	188.46	0.244	1.27	483.46	0.236	1.39
$C_{L_{\max}} = 1.5$	351.67	0.277	1.30	167.70	0.246	1.25	419.19	0.254	1.37
$C_{L_{\max}} = 1.7$	310.52	0.295	1.25	150.21	0.250	1.23	366.34	0.271	1.32

Table 3 Optimized drogue orbit radius and corresponding cable stability

Case	Orion			Light aircraft			Fighter		
	r_d, m	Max. real part of λ	Cable extension, m	r_d, m	Max. real part of λ	Cable extension, m	r_d, m	Max. real part of λ	Cable extension, m
Baseline	3.28	−0.0698	2.28	1.48	−0.0669	2.29	6.18	−0.0720	2.99
$m_d = 50$ kg	5.78	−0.1046	2.36	3.54	−0.0856	3.16	11.32	−0.1089	2.81
$m_d = 100$ kg	7.22	−0.1284	2.41	5.79	−0.1115	4.49	13.74	−0.1347	2.72
$m_d = 500$ kg	11.96	−0.1240	2.73	——	——	——	20.39	−0.1603	2.73
$C_D A_d = 0.5$ m^2	3.76	−0.0901	2.40	1.53	−0.0736	2.32	8.68	−0.1023	3.38
$C_D A_d = 1.0$ m^2	3.61	−0.0819	2.34	1.52	−0.0715	2.30	7.59	−0.0875	3.13
$C_D A_d = 3.0$ m^2	3.00	−0.0618	2.25	1.44	−0.0623	2.27	5.33	−0.0633	2.96
$L = 1$ km	22.93	−0.0907	2.99	6.11	−0.0947	0.24	48.29	−0.1311	2.97
$L = 2$ km	7.33	−0.0739	2.13	2.45	−0.0781	1.01	13.38	−0.0741	4.62
$L = 4$ km	1.91	−0.0641	3.75	1.15	−0.0608	4.09	3.53	−0.0668	3.81
$L = 5$ km	1.34	−0.0595	5.80	1.05	−0.0569	6.30	2.38	−0.0622	5.61
$\phi_{\max} = 40$ deg	18.34	−0.0902	1.31	4.14	−0.0676	1.62	30.25	−0.0952	4.04
$\phi_{\max} = 50$ deg	10.68	−0.0781	1.38	1.85	−0.0667	2.02	17.03	−0.0864	2.14
$\phi_{\max} = 60$ deg	6.38	−0.0715	1.70	1.48	−0.0669	2.29	10.43	−0.0774	2.17
$C_{L_{\max}} = 1.3$	2.04	−0.0690	2.23	1.47	−0.0639	2.31	3.65	−0.0701	2.32
$C_{L_{\max}} = 1.5$	1.38	−0.0688	2.30	1.39	−0.0639	2.36	2.30	−0.0692	2.22
$C_{L_{\max}} = 1.7$	1.00	−0.0691	2.43	1.28	−0.0650	2.42	1.55	−0.0689	2.27

Optimal configurations were generated for a range of cases by varying some of the key system parameters. The base system parameters were selected as $m_d = 10$ kg, $L = 3000$ m, $C_D A_d = 2$ m^2, $\phi_{\max} = 70$ deg, $C_{L_{\max}} = 1.1$, and $n_{\max} = 4$. A total of 17 different variations of parameters were used, and the results are summarized in Tables 2 and 3. Note that variations in $C_{L_{\max}}$ are associated with increments of C_{D_0} given by $\Delta C_{D_0} = 0.1 \Delta C_{L_{\max}}$.

Table 2 shows the optimal orbit radius of the aircraft, its angular velocity, and cable diameter required to sustain the loads induced by the maneuver. Note that no solution was obtained for the light aircraft towing a payload of 500 kg. The least massive cable (smallest diameter) is required for a 1 km long cable towed by the Orion aircraft, whereas the heaviest cable is needed to tow a payload of 500 kg at the nominal length of 3 km. The trend in the optimal results also suggests that as the payload mass is increased, the towing radius should also be increased. For example, an Orion aircraft towing only 10 kg should fly a 468 m radius circle, whereas a radius of 497.2 m is needed to optimally tow 500 kg. A similar trend is observed for the fighter-type aircraft. The drag on the drogue does not appear to be a particularly sensitive parameter for the optimized configurations. For example, as the product $C_D A_d$ is varied from 0.5 to 3 m^2, the required aircraft orbit radius and angular velocity are largely unchanged, and the cable diameter varies only slightly. This should be contrasted with the dramatic effect of cable length on the optimal solutions, as well as the aircraft performance constraints. A longer cable is preferable from the point-of-view that the required orbit radius of the aircraft increases. Increasing the maximum aircraft lift coefficient, possibly through the use of high-lift devices, leads to smaller circles, thereby improving the stationary motion. Finally, the maximum bank angle for the aircraft severely limits the achievable towpoint radius, which has the most physical difference for the fighter-type aircraft, i.e., for 40 deg maximum bank the aircraft radius is 816 m, whereas for 60 deg maximum bank the required radius reduces to 614 m. It is also important to point out that the load factor constraint does not play a role in any of the results presented in this paper. That is, the maximum load factor always appears to be less than 3, which is much lower than the upper bound of 4.

Table 3 shows the optimal drogue orbit radius for the parameters given in Table 2. For the baseline system, a light aircraft configuration can achieve the smallest orbit radius of the drogue. This is supported by the results shown in Fig. 4. An orbit radius of approximately 1.5 m (0.69% of aircraft radius) can be achieved using the light aircraft, whereas the Orion aircraft can achieve approximately 3.3 m (0.70% of aircraft radius). Table 3 clearly shows that the fighter-type aircraft is a poor choice for such a maneuver. An Orion-like aircraft is nearly twice as good in terms of the achievable drogue radius in the optimal configuration. It must also be noted that Table 3 shows that all optimal configurations are dynamically stable. That is, the real parts of all eigenvalues λ are less than zero. The ability to pickup large payloads is limited because of the achievable orbit radius versus changes in the drogue mass. For example, whereas a drogue mass of 10 kg can be towed in a radius of 3.28 m, a mass of 500 kg can be towed in a circle of 11.96 m for the Orion aircraft. In addition to this, the cable diameter to tow the 500 kg payload must be 5.85 times thicker than the cable needed to tow 10 kg. Although not conducted here, the cable thickness needed for the largest expected payload would have to be fixed and the optimal towing radii recalculated for the range of payloads expected for the system. Table 3 also shows that the stability of the cable increases as the payload mass is increased in the optimal configuration, whereas increasing the drag properties of the drogue decreases the stability of the least stable mode. This can be understood physically by considering that increasing the drag properties means that it would take longer for the drogue to return to equilibrium after being displaced because of the higher ratio of drag to inertial forces. Furthermore, increasing the drag properties of the drogue does not lead to a significant benefit in terms of the optimal drogue tow radius. This appears to be particularly true for the light aircraft configuration, where only a few centimeters difference is observed. As is well known in the literature, there is a ratio of cable length to towpoint

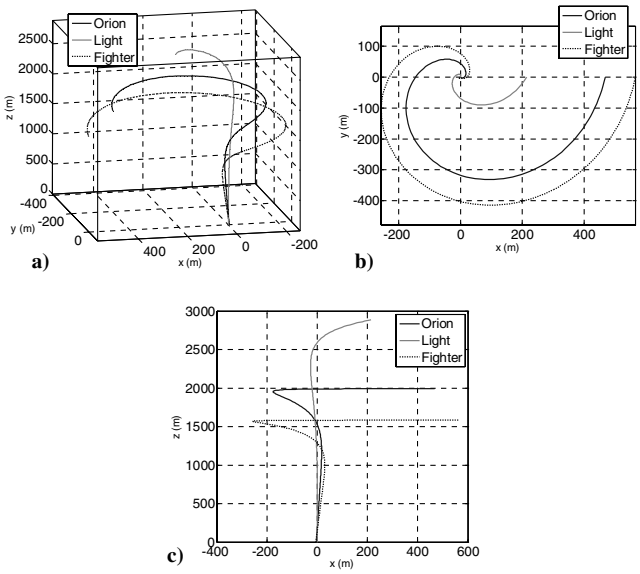

Fig. 5 Optimal cable configurations for baseline system: a) 3-D plot, b) projection in horizontal plane, and c) projection in vertical plane.

radius that results in a significant improvement in the drogue tow radius. This is important for aircraft because of the physical limitations of the aircraft performance characteristics. This result can be observed in Table 3 for the variations in cable length. For example, a 1 km long cable, which gives $r/L \approx 0.5$, is too short to achieve the type of performance required for this system. In addition to this, continually increasing the cable length does not lead to significantly better designs. Increases in cable length mean thicker, heavier cables. The results suggest that a cable length on the order of 2–4 km would be best. Finally, as was noted previously, the two most critical aircraft parameters are the maximum thrust (or power) and the maximum bank angle. However, for the light aircraft configuration, much lower bank angles are tolerable for acceptable drogue tow radii. In particular, the nominal optimal configuration is limited by available power, not the bank angle (52.7 deg required). Table 3 also gives the longitudinal extension of the cable for each of the cases. The typical strain in the cable is on the order of 0.1% for the selected parameters. This elongation is virtually insignificant compared with other external forces acting on the system, such as wind loads, and could be neglected. However, for other materials with lower Young's

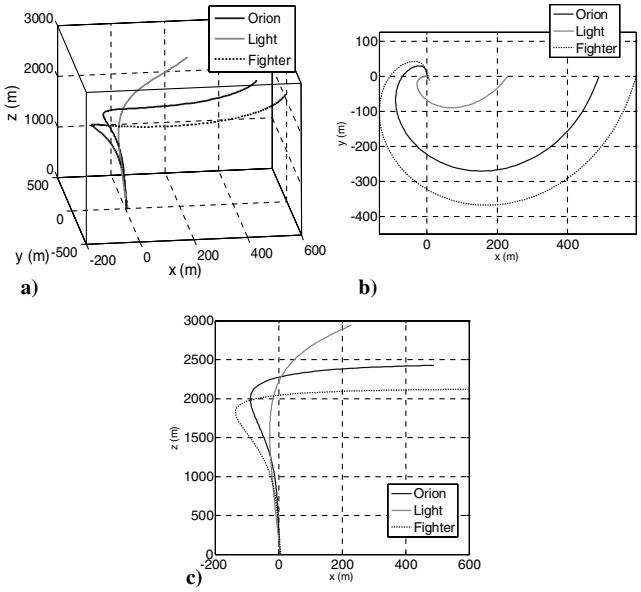

Fig. 6 Optimal cable configurations for 100 kg drogue system: a) 3-D plot, b) projection in horizontal plane, and c) projection in vertical plane.

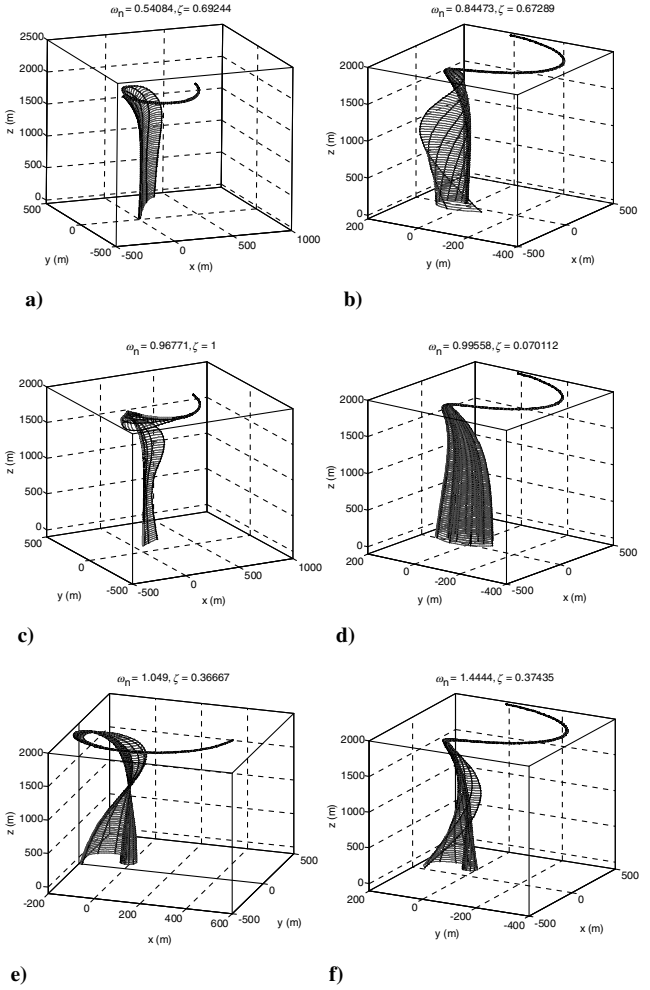

Fig. 7 Fundamental modes of cable vibrations for Orion baseline system, showing modes a) 1, b) 2, c) 3, d) 4, e) 5, and f) 6.

modulus such as nylon, the cable extension is significant for larger loads. Treating the cable elasticity, however, renders the equations of motion simpler (no constraint equations) and allows the influence of longitudinal vibrations to be taken into account in stability computations.

Figure 5 shows the cable shapes for the optimal system configurations for each aircraft using the baseline system parameters. This exemplifies the difference that the aircraft selection plays on the optimal system configuration. It can be seen that the actual aircraft altitude for the same length cable is a function of the aircraft orbit radius and speed. For example, the fighter has the largest orbit radius and least altitude (1.586 km), whereas the light aircraft has the smallest orbit radius and highest altitude (2.885 km). Furthermore, there is quite a significant difference in the cable shape for each aircraft case. The larger radius and higher speed cases (Orion and fighter) tend to result in a nearly horizontal cable at the aircraft attachment point, whereas the slower moving light aircraft has most of its cable in the vertical plane. It is interesting to note the significantly different configurations for similar drogue orbit radii. Increasing the drogue mass to 100 kg has a fairly significant impact on the equilibrium configurations, as shown in Fig. 6. The largest effect is on the aircraft altitude. For example, the required altitude for the fighter with a 100 kg drogue increases by 534 m from the nominal 10 kg case, whereas the light aircraft altitude increases by 58 m. This has serious implications for payload pickup, which causes changes in the drogue mass. It is likely that the aircraft would need to change altitude after picking up a payload to help alleviate transient forces that would be induced by the sudden change from equilibrium.

The solution of the eigenvalue problem, as well as providing details of the system stability, also provides information on the system vibration modes. Typically, we are interested in the fundamental modes of the system, which correspond to the modes of lowest frequency. The first six modes for the Orion aircraft are shown in Fig. 7 with the damping and natural frequencies of each mode indicated at the top of each plot. Note that the natural frequencies are nondimensional due to the choice of angle as the independent variable as opposed to time. The plots show the equilibrium configuration (thick gray line) with a time varying modal response (black dots show some discrete points on the cable, and the thin lines show the time evolution of the point) superimposed. The time response of the particular mode is shown for two periods. Figure 7a shows the fundamental mode of vibration, which is dominated by motion of the lower portion of the cable, i.e., there is negligible motion of the portion of the cable that is nearly horizontal closest to the aircraft. The mode is characterized by a rigid body like movement of the cable tip in the y–z-plane, with small oscillatory motion in the x–z-plane. The second mode has similar damping to the first mode, but is characterized by a rigid body spiraling motion of the drogue. The third mode is a nonoscillatory rigid body motion of the drogue in the y–z-plane. The fourth mode is a very lightly damped spiraling motion of the drogue. The fifth and sixth modes are spiraling motion of the drogue, combined with stringlike vibrations of the cable, which are well damped and appear to act like a rigid body "twisting" of the cable when viewed in the rotating frame.

The modal response of the cable for the light aircraft baseline configuration is shown in Fig. 8. Comparing these results with those from the Orion configuration (Fig. 7) shows that the modal responses are quite different both qualitatively and in terms of frequency and damping. The first two modes for the light aircraft are of higher frequency and lower damping than the first two modes for the Orion configuration. In particular, the first two modes for the light aircraft appear to be combinations of spiraling motion of the drogue

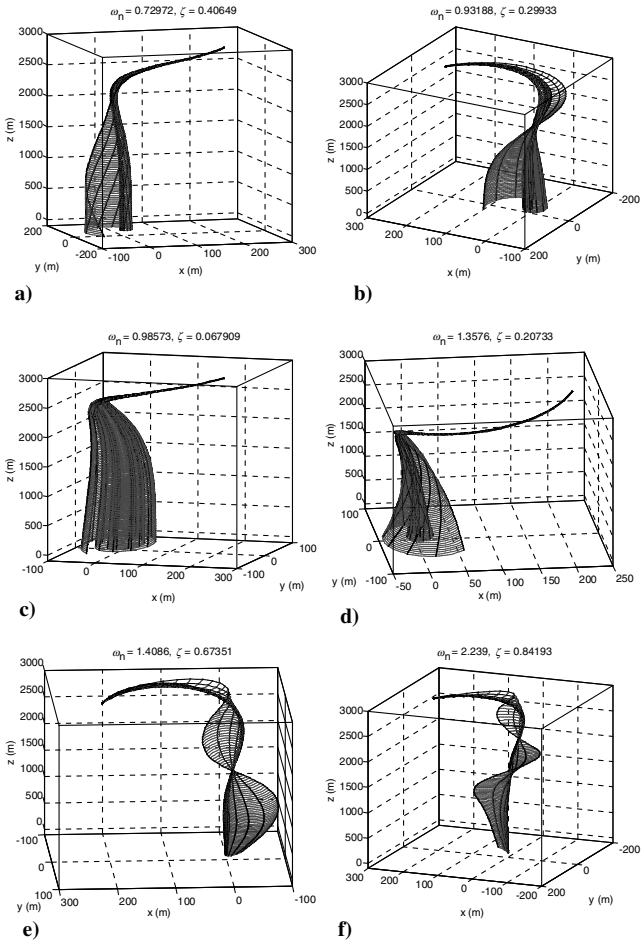

Fig. 8 Fundamental modes of cable vibrations for light aircraft baseline system, showing modes a) 1, b) 2, c) 3, d) 4, e) 5, and f) 6.

and lateral stringlike modes of the cable. The third mode is a rigid body, lightly damped spiraling motion of the drogue (compare with Orion's fourth mode). The fourth mode combines the spiraling mode with cable lateral bending or twirling. Finally, the fifth and sixth modes, which are damped quite well, are largely lateral string modes. Note the two "nodes" in the fifth mode, and three nodes in the sixth mode.

The major reason for the difference in modal response is naturally due to the different operating conditions, which affects the ratio of aerodynamic forces to inertial forces. This leads to quite different equilibrium configurations, affecting the responses. The light aircraft configuration has most of the cable nearly vertical, whereas the Orion configuration has a large portion of the cable nearly horizontal. The horizontal portions of the cable are due to the large drag forces caused by the large distance of the cable from the axis of rotation at these points. A typical simulation of the system with the cable initially hanging suggests that the lightly damped rigid body spiraling motion of the drogue dominates the response. This mode takes considerable time to damp out and may limit the application of the method for picking up payloads unless some kind of anchoring system is used, particularly in the face of gusts and other disturbances. Numerical results from the different parameter variations also suggest that the damping of this mode is increased if the $C_D A_d$ product is reduced. This is at the cost of a slightly higher drogue orbit radius.

As part of our desire to develop this technology to an automated system including winch control and an automatic flight controller [37], a flight test using a model aircraft was performed to qualitatively verify some of the effects seen in simulations during circularly towed motion. A model aircraft towing 100 m of cord was used. The aircraft was manually controlled during the tests so it proved difficult to obtain good, steady configurations for long periods of time. In addition, the presence of a crosswind required some special attention by the pilot. In the best operating conditions achieved during the tests, the end of the cable was lowered and remained stationary on the ground where it was handled by observers as the aircraft continued circling above. This configuration was achieved for approximately 8 min.

One of the limitations of the results shown in this paper is that the atmosphere is assumed to be motionless relative to the system. The presence of a steady crosswind has a significant effect on the solutions, causing both lateral and vertical deviations of the cable tip. The methods of analysis used here cannot be directly applied to such cases because the cable no longer takes up a quasi-steady shape. Instead, periodic solutions of the cable in the rotating frame are obtained [38]. Some of these effects, as well as possible solutions involving cable winch control and flying the aircraft in slightly elliptic orbits upwind of the target point are discussed in [38,39]. Alternatively, anchoring of the cable tip at the ground would allow accurate payload retrieval and positioning of the cable tip. This possibility merits further study.

VI. Conclusions

The equilibrium, performance, and stability of an aircraft towed-cable system has been studied for the case where the aircraft flies a circular orbit at high altitude. For long cables, the drogue takes up a position close to the center of the circle and appears nearly stationary in an inertial frame. Equilibrium configurations were determined using a lumped parameter discretization of the cable combined with an inverse approach. The equilibrium and stability of practical configurations for three different aircraft resembling a P-3C Orion, a general light aircraft, and a military fighter were obtained. In the general case, the achievable configurations are restricted by the aircraft maximum lift coefficient, bank angle, and thrust or power available. Optimal configurations, defined as ones that give the smallest orbit radius of the drogue, were determined by solving a constrained optimization problem. It is possible to achieve a cable tip motion with a radius of approximately 1.5 m using a light aircraft towing a 3 km long cable. The resulting velocity of the cable tip is approximately 0.36 m/s. The stability of the resulting optimal configurations was studied by numerically linearizing the governing equations and solving a large-scale eigenvalue problem. A modal analysis shows that the response of the system is dominated by lightly damped, low frequency modes mostly influencing the position of the drogue.

Appendix A: Nondimensional Equations of Motion

The nondimensional equations of motion for cable are expressed in the following form:

$$\begin{aligned}\Lambda_n'' = {} & -\frac{r}{L}\sin\alpha_n + \Lambda_n\beta_n'^2\cos^2\alpha_n - \Lambda_n\cos^2\alpha_n\cos^2\beta_n + \Lambda_n\alpha_n'^2 \\ & + \Lambda_n - 2\Lambda_n\alpha_n'\sin\beta_n + 2\Lambda_n\beta_n'\sin\alpha_n\cos\alpha_n\cos\beta_n \\ & - \frac{F^{\text{total}}_{3(n-1)+1}}{m_n L\dot\theta^2}\sin\alpha_n - \frac{F^{\text{total}}_{3(n-1)+2}}{m_n L\dot\theta^2}\cos\alpha_n\sin\beta_n \\ & - \frac{F^{\text{total}}_{3(n-1)+3}}{m_n L\dot\theta^2}\cos\alpha_n\cos\beta_n \end{aligned} \tag{A1}$$

$$\begin{aligned}\Lambda_j'' = {} & \Lambda_j\beta_j'^2\cos^2\alpha_j - \Lambda_j\cos^2\alpha_j\cos^2\beta_j + \Lambda_j\alpha_j'^2 + \Lambda_j \\ & - 2\Lambda_j\alpha_j'\sin\beta_j + 2\Lambda_j\beta_j'\sin\alpha_j\cos\alpha_j\cos\beta_j \\ & + \left(\frac{F^{\text{total}}_{3j+1}}{m_{j+1}L\dot\theta^2} - \frac{F^{\text{total}}_{3(j-1)+1}}{m_j L\dot\theta^2}\right)\sin\alpha_j \\ & + \left(\frac{F^{\text{total}}_{3j+2}}{m_{j+1}L\dot\theta^2} - \frac{F^{\text{total}}_{3(j-1)+2}}{m_j L\dot\theta^2}\right)\cos\alpha_j\sin\beta_j \\ & + \left(\frac{F^{\text{total}}_{3j+3}}{m_{j+1}L\dot\theta^2} - \frac{F^{\text{total}}_{3(j-1)+3}}{m_j L\dot\theta^2}\right)\cos\alpha_j\cos\beta_j \end{aligned} \tag{A2}$$

$$\begin{aligned}\alpha_n'' = {} & -\frac{r}{\Lambda_n L}\cos\alpha_n - 2\frac{\Lambda_n'\alpha_n'}{\Lambda_n} + 2\frac{\Lambda_n'}{\Lambda_n}\sin\beta_n + 2\beta_n'\cos^2\alpha_n\cos\beta_n \\ & + \sin\alpha_n\cos\alpha_n\cos^2\beta_n - \beta_n'^2\sin\alpha_n\cos\alpha_n - \frac{F^{\text{total}}_{3(n-1)+1}}{m_n\Lambda_n L\dot\theta^2}\cos\alpha_n \\ & + \frac{F^{\text{total}}_{3(n-1)+2}}{m_n\Lambda_n L\dot\theta^2}\sin\alpha_n\sin\beta_n + \frac{F^{\text{total}}_{3(n-1)+3}}{m_n\Lambda_n L\dot\theta^2}\sin\alpha_n\cos\beta_n \end{aligned} \tag{A3}$$

$$\begin{aligned}\alpha_j'' = {} & -2\frac{\Lambda_j'\alpha_j'}{\Lambda_j} + 2\frac{\Lambda_j'}{\Lambda_j}\sin\beta_j + 2\beta_j'\cos^2\alpha_j\cos\beta_j \\ & + \sin\alpha_j\cos\alpha_j\cos^2\beta_j - \beta_j'^2\sin\alpha_j\cos\alpha_j \\ & + \left(\frac{F^{\text{total}}_{3j+1}}{m_{j+1}\Lambda_j L\dot\theta^2} - \frac{F^{\text{total}}_{3(j-1)+1}}{m_j\Lambda_j L\dot\theta^2}\right)\cos\alpha_j \\ & + \left(\frac{F^{\text{total}}_{3(j-1)+2}}{m_j\Lambda_j L\dot\theta^2} - \frac{F^{\text{total}}_{3j+2}}{m_{j+1}\Lambda_j L\dot\theta^2}\right)\sin\alpha_j\sin\beta_j \\ & + \left(\frac{F^{\text{total}}_{3(j-1)+3}}{m_j\Lambda_j L\dot\theta^2} - \frac{F^{\text{total}}_{3j+3}}{m_{j+1}\Lambda_j L\dot\theta^2}\right)\sin\alpha_j\cos\beta_j \end{aligned} \tag{A4}$$

$$\begin{aligned}\beta_n'' = {} & -2\frac{\Lambda_n\beta_n'}{\Lambda_n} - 2\frac{\Lambda_n'\sin\alpha_n\cos\beta_n}{\Lambda_n\cos\alpha_n} + 2\frac{\alpha_n'\beta_n'\sin\alpha_n}{\cos\alpha_n} \\ & + \sin\beta_n\cos\beta_n - 2\alpha_n'\cos\beta_n - \frac{F^{\text{total}}_{3(n-1)+2}}{m_n\Lambda_n L\dot\theta^2}\frac{\cos\beta_n}{\cos\alpha_n} \\ & + \frac{F^{\text{total}}_{3(n-1)+3}}{m_n\Lambda_n L\dot\theta^2}\frac{\sin\beta_n}{\cos\alpha_n} \end{aligned} \tag{A5}$$

$$\beta_j'' = -2\frac{\Lambda_j'\beta_j'}{\Lambda_j} - 2\frac{\Lambda_j' \sin\alpha_j \cos\beta_j}{\Lambda_j \cos\alpha_j} + 2\frac{\alpha_j'\beta_j' \sin\alpha_j}{\cos\alpha_j} + \sin\beta_j \cos\beta_j - 2\alpha_j' \cos\beta_j + \left(\frac{F_{3j+2}^{\text{total}}}{m_{j+1}\Lambda_j L\dot{\theta}^2} - \frac{F_{3(j-1)+2}^{\text{total}}}{m_j\Lambda_j L\dot{\theta}^2}\right)\frac{\cos\beta_j}{\cos\alpha_j} + \left(\frac{F_{3(j-1)+3}^{\text{total}}}{m_j\Lambda_j L\dot{\theta}^2} - \frac{F_{3j+3}^{\text{total}}}{m_{j+1}\Lambda_j L\dot{\theta}^2}\right)\frac{\sin\beta_j}{\cos\alpha_j} \tag{A6}$$

In this paper, L is selected to be equal to L_{s_j}.

Appendix B: Central Finite Differences for Linear Stability Analysis

The general nonlinear equations of motion are represented in the state-space form

$$\dot{\boldsymbol{x}} = \boldsymbol{f}(\boldsymbol{x}) \tag{B1}$$

where $\boldsymbol{x} = [\Lambda_1, \alpha_1, \beta_1, \ldots, \Lambda_n, \alpha_n, \beta_n, \Lambda_1', \alpha_1', \beta_1', \ldots, \Lambda_n', \alpha_n', \beta_n']^\top$ is the state vector. The nonlinear equations may be expressed in the linearized form around a given equilibrium position as

$$\delta\dot{\boldsymbol{x}} = \boldsymbol{A}\delta\boldsymbol{x} \tag{B2}$$

where $\delta\boldsymbol{x}$ is a small perturbation of the states around the equilibrium position, and $\boldsymbol{A}$ is the linear state matrix defined by

$$\boldsymbol{A} = \begin{bmatrix} \frac{\partial f_1}{\partial x_1} & \cdots & \frac{\partial f_1}{\partial x_{6n}} \\ \vdots & \ddots & \vdots \\ \frac{\partial f_{6n}}{\partial x_1} & \cdots & \frac{\partial f_{6n}}{\partial x_{6n}} \end{bmatrix} \tag{B3}$$

The partial derivatives in Eq. (B3) are obtained by way of the central difference approximation

$$\frac{\partial f_i}{\partial x_j} \approx \frac{f_i(x_j + \Delta x_j) - f_i(x_j - \Delta x_j)}{2\Delta x_j} \tag{B4}$$

where the value of the perturbation depends on the reference value of the parameter according to

$$\Delta x_j = \bar{\delta}(1 + 10^{-3}|x_j|) \tag{B5}$$

where $\bar{\delta}$ is a small perturbation (10^{-6} is used). The validity of the linearization was tested using an approach similar to that of Lambert and Nahon [40]. The linear equations and nonlinear equations may be integrated for a small perturbation and if the corresponding numerical results are in good agreement then it may be concluded that the linearization process has been accurately performed.

Acknowledgment

We would like thank Peter Lapthorne for supplying and flying the model aircraft used in the preliminary flight tests.

References

[1] Jun, Y.-W., Hall, K. R., Bennett, A. G., and Bridges, P. D., "Optimal Guidance for Airborne Cable Pickup System," AIAA Paper 84-1893, Aug. 1984.

[2] Trivailo, P., Sgarioto, D., and Blanksby, C., "Optimal Control of Aerial Tethers for Payload Rendezvous," *The 5th Asian Control Conference*, Vol. 2, Melbourne, Australia, July 2004, pp. 396–404.

[3] Williams, P., Sgarioto, D., and Trivailo, P., "Optimal Control of an Aircraft-Towed Flexible Cable System," *Journal of Guidance, Control, and Dynamics*, Vol. 29, No. 2, 2006, pp. 401–410.

[4] Kolodner, I., "Heavy Rotating String—A Nonlinear Eigenvalue Problem," *Communications on Pure and Applied Mathematics*, Vol. 9, No. 3, 1955, pp. 334–338.

[5] Wu, C. H., "Whirling of a String at Large Angular Speeds—A Nonlinear Eigenvalue Problem with Moving Boundary Layers," *SIAM Journal on Applied Mathematics*, Vol. 22, No. 1, 1972, pp. 1–13.

[6] Caughey, T. K., "Whirling of a Heavy Chain," *Proceedings of the 3rd U.S. National Congress of Applied Mechanics*, American Society of Mechanical Engineers, New York, 1958, pp. 101–108.

[7] Coomer, J., Lazarus, M., Tucker, R. W., Kershaw, D., and Tegman, A., "A Non-Linear Eigenvalue Problem Associated with Inextensible Whirling Strings," *Journal of Sound and Vibration*, Vol. 239, No. 5, 2001, pp. 969–982.

[8] Lemon, G., and Fraser, W. B., "Steady-State Bifurcations and Dynamical Stability of a Heavy Whirling Cable Acted on by Aerodynamic Drag," *Proceedings of the Royal Society of London A*, Vol. 457, May 2001, pp. 1021–1041.

[9] Skop, R. A., and Choo, Y.-I., "The Configuration of a Cable Towed in a Circular Path," *Journal of Aircraft*, Vol. 8, No. 11, 1971, pp. 856–862.

[10] Russell, J. J., and Anderson, W. J., "Equilibrium and Stability of a Whirling Rod-Mass System," *International Journal of Non-Linear Mechanics*, Vol. 12, No. 2, 1977, pp. 91–101.

[11] Russell, J. J., and Anderson, W. J., "Equilibrium and Stability of a Circularly Towed Cable Subject to Aerodynamic Drag," *Journal of Aircraft*, Vol. 14, No. 7, 1977, pp. 680–686.

[12] Zhu, F., and Rahn, C. D., "Stability Analysis of a Circularly Towed Cable-Body System," *Journal of Sound and Vibration*, Vol. 217, No. 3, 1998, pp. 435–452.

[13] Cohen, Y., and Manor, H., "Equilibrium Configurations of a Cable Drogue System Towed in a Helical Motion," *International Journal of Engineering Science*, Vol. 26, No. 8, 1988, pp. 771–786.

[14] Zhu, F., Hall, K., and Rahn, C. D., "Steady State Response and Stability of Ballooning Strings in Air," *International Journal of Non-Linear Mechanics*, Vol. 33, No. 1, 1998, pp. 33–46.

[15] Narkis, Y., "Deployment Forces in Towing Systems," *Journal of Aircraft*, Vol. 15, No. 2, 1978, pp. 123–124.

[16] Matuk, C., "Flight Tests of Tow Wire Forces While Flying a Racetrack Pattern," *Journal of Aircraft*, Vol. 20, No. 7, 1983, pp. 623–627.

[17] Crist, S. A., "Analysis of the Motion of a Long Wire Towed from an Orbiting Aircraft," *Shock and Vibration Bulletin*, Vol. 41, No. 6, 1970, pp. 61–73.

[18] Clifton, J. M., Schmidt, L. V., and Stuart, T. D., "Dynamic Modeling of a Trailing Wire Towed by an Orbiting Aircraft," *Journal of Guidance, Control, and Dynamics*, Vol. 18, No. 4, 1995, pp. 875–881.

[19] Schram, J. W., and Reyle, S. P., "A Three-Dimensional Dynamic Analysis of a Towed System," *Journal of Hydronautics*, Vol. 2, No. 4, 1968, pp. 213–220.

[20] Ablow, C. M., and Schechter, S., "Numerical Simulation of Undersea Cable Dynamics," *Ocean Engineering*, Vol. 10, No. 6, 1983, pp. 443–457.

[21] Roberts, G. M., Connell, H. J., and May, R. L., "A Three Dimensional Model of a Towed Cable-Body System," RMIT Dept. of Mathematics Research Report No. 14, Melbourne, Australia, Aug. 1994.

[22] Chin, C. K. H., May, R. L., and Connell, H. J., "A Numerical Model of a Towed Cable-Body System," *ANZIAM Journal*, Vol. 42, Pt. E, 2000, pp. C362–C384.

[23] Pai, P. F., and Nayfeh, A. H., "Fully Nonlinear Model of Cables," *AIAA Journal*, Vol. 30, No. 12, 1992, pp. 2993–2996.

[24] Leonard, J. W., and Nath, J. H., "Comparison of Finite Element and Lumped Parameter Methods for Oceanic Cables," *Engineering Structures*, Vol. 3, No. 3, 1981, pp. 153–167.

[25] Driscoll, R., and Nahon, M., "Mathematical Modeling and Simulation of a Moored Buoy System," *Proceedings of IEEE Oceans*, Vol. 1, Sept. 1996, pp. 517–523.

[26] Buckham, B., Nahon, M., and Seto, M., "Three-Dimensional Dynamics Simulation of a Towed Underwater Vehicle," American Society of Mechanical Engineers Paper 99-3068, 1999.

[27] Winget, J. M., and Huston, R. L., "Cable Dynamics—A Finite Segment Approach," *Computers and Structures*, Vol. 6, No. 6, 1976, pp. 475–480.

[28] Kamman, J. W., and Huston, R. L., "Modeling of Variable Length Towed and Tethered Cable Systems," *Journal of Guidance, Control, and Dynamics*, Vol. 22, No. 4, 1999, pp. 602–608.

[29] Banerjee, A. K., and Do, V. N., "Deployment Control of a Cable Connecting a Ship to an Underwater Vehicle," *Applied Mathematics and Computation*, Vol. 70, Nos. 2–3, 1995, pp. 97–116.

[30] Dreyer, T. P., and Murray, D. M., "On the Modeling of Two-Dimensional Segmented Representations of Cable Shape," *Ocean Engineering*, Vol. 11, No. 6, 1984, pp. 609–625.

[31] Choo, Y.-I., and Casarella, M. J., "A Survey of Analytical Methods for Dynamic Simulation of Cable-Body Systems," *Journal of Hydronautics*, Vol. 7, No. 4, 1973, pp. 137–144.
[32] Hoerner, S. F., *Fluid-Dynamic Drag*, Hoerner Fluid Dynamics, Bakersfield, CA, 1965.
[33] Cochran, J. E., Innocenti, M., No, T. S., and Thukral, A., "Dynamics and Control of Maneuverable Towed Flight Vehicles," *Journal of Guidance, Control, and Dynamics*, Vol. 15, No. 5, 1992, pp. 1245–1252.
[34] Gill, P. E., Murray, W., and Saunders, M. A., "SNOPT: An SQP Algorithm for Large-Scale Constrained Optimization," *SIAM Journal on Optimization*, Vol. 12, No. 4, 2002, pp. 979–1006.
[35] Murray, R. M., "Trajectory Generation for a Towed Cable System using Differential Flatness," *IFAC World Congress*, Pergamon, New York, 1996, pp. 395–400.
[36] Williams, P., and Trivailo, P., "Cable Deployment Control for Towed Aerial-Cable Payload Pick-Up and Delivery System," *Proceedings of the Land Warfare Conference*, edited by V. Puri, D. Filippidis, P. Retter, and J. Kelly, Defense Science and Technology Office, Melbourne, Australia, 2004, pp. 313–329.
[37] Hambling, D., "Throw Me a Rope," *New Scientist*, Vol. 2497, April 2005, pp. 35–37.
[38] Williams, P., and Trivailo, P., "Periodic Solutions for Flexible Cable-Body Systems Towed in Circular and Elliptical Paths," AIAA Paper 2006-6374, Aug. 2006.
[39] Williams, P., "Optimal Control of a Circularly-Towed Aerial-Cable System in Presence of Cross-Wind," AIAA Paper 2006-6192, Aug. 2006.
[40] Lambert, C., and Nahon, M., "Stability Analysis of a Tethered Aerostat," *Journal of Aircraft*, Vol. 40, No. 4, 2003, pp. 705–715.